Anharmonic electron-phonon coupling in ultrasoft and locally disordered perovskites

Marios Zacharias, George Volonakis, Feliciano Giustino, Jacky Even

npj computational materials

www.nature.com/npjcompumats

ARTICLE OPEN

Anharmonic electron-phonon coupling in ultrasoft and locally disordered perovskites

Marios Zacharias[1]✉, George Volonakis[2], Feliciano Giustino[3,4] and Jacky Even[1]✉

Anharmonicity and local disorder (polymorphism) are ubiquitous in perovskite physics, inducing various phenomena observed in scattering and spectroscopy experiments. Several of these phenomena still lack interpretation from first principles since, hitherto, no approach is available to account for anharmonicity and disorder in electron–phonon couplings. Here, relying on the special displacement method, we develop a unified treatment of both and demonstrate that electron–phonon coupling is strongly influenced when we employ polymorphous perovskite networks. We uncover that polymorphism in halide perovskites leads to vibrational dynamics far from the ideal noninteracting phonon picture and drives the gradual change in their band gap around phase transition temperatures. We also clarify that combined band gap corrections arising from disorder, spin-orbit coupling, exchange–correlation functionals of high accuracy, and electron–phonon coupling are all essential. Our findings agree with experiments, suggesting that polymorphism is the key to address pending questions on perovskites' technological applications.

npj Computational Materials (2023)9:153 ; https://doi.org/10.1038/s41524-023-01089-2

INTRODUCTION

Oxide perovskites are fascinating materials with extensive applications owing to their intrinsic ferroelectric, antiferroelectric, and piezoelectric properties[1]. Halide perovskites are of high interest due to their impressive efficiencies in solar cells[2,3], and attractive applications in optoelectronics, electrocatalysis, and thermoelectrics[4–6]. Our understanding of perovskites' key properties is connected to deviations of the vibrational dynamics and electron–phonon coupling from the standard picture observed in conventional semiconductors[7,8]. For example, halide perovskites exhibit (i) ultralow thermal conductivities attributed to their low-energy vibrational densities and peculiar anharmonic characteristics[9,10] and (ii) limited carrier mobilities which have been discussed in terms of electron–phonon Fröhlich coupling[11], dipolar scattering arising from anharmonic halide motion[12], and polaronic transport[13].

A signature of strong anharmonicity in tetragonal or cubic perovskites (stoichiometry ABX_3) is the multi-well potential energy surface (PES), U, described by nuclei displacements, $\Delta\tau$, away from their static-equilibrium positions (Fig. 1a). Static-equilibrium geometries occur when the net force on each atom vanishes, giving rise to local extrema in the PES. The high-symmetry idealized geometry, also referred to as monomorphous structure[14], corresponds to a local maximum; it features perfectly aligned octahedra and can be described by a reference unit cell composed of a few atoms. Local minima are explored when the nuclei move away from their high-symmetry positions, forming a locally disordered (or polymorphous) network characterized by tilted BX_3 octahedra and a distorted configuration of the A cations (Fig. 1a). Description of this form of static or quasi-static (vide infra) disorder requires supercells that can accommodate symmetry-breaking domains between the repeated unit cells.

Typical density functional theory (DFT) calculations of tetragonal or cubic perovskites rely on the assumption of a high-symmetry network, disregarding the locally disordered ground state configurations. This assumption misses important corrections to the electronic structure[14,15] and requires enforcing the crystal's symmetries on anharmonic phonon dynamics[16], thus, represented by idealized well-defined dispersions. Such behavior is disconnected from measurements of overdamped optical vibrations, structural disorder, and complex pretransitional dynamics close to structural phase transitions[17–26]. Furthermore, direct evidence of local disorder in cubic perovskites is observed in measurements of pair distribution functions (PDFs), Bragg diffraction, and extended diffuse scattering[23,27–31].

In this work we demonstrate the important role of anharmonicity and local disorder in the electronic structure, phonon dynamics, and electron–phonon coupling of oxide and halide perovskites ($SrTiO_3$, $CsPbBr_3$, $CsPbI_3$, and $CsSnI_3$). Hybrid halide perovskites undergo additional relaxations related to molecular reorientations, but as a proof of concept we here focus on inorganic compounds. We show from first-principles that (i) local disorder and anharmonicity are at the origin of overdamped and strongly coupled phonons; (ii) local disorder and anharmonicity are essential to describe electron–phonon coupling; (iii) low-energy anharmonic optical vibrations dominate thermal band gap renormalization; (iv) local disorder is the key to explain the smooth evolution of the band gap with temperature around phase transitions; (v) a full description of band gaps and effective masses requires combining disorder with fully relativistic effects. To address points (i)–(iv), we employ a recently developed approach, namely anharmonicity via the special displacement method (A-SDM)[32], that allows the unified treatment of anharmonic electron–phonon coupling. Our study calls for revisiting open questions related to electron–phonon and anharmonic properties of halide and oxide perovskites.

[1]Univ Rennes, INSA Rennes, CNRS, Institut FOTON - UMR 6082, F-35000 Rennes, France. [2]Univ Rennes, ENSCR, INSA Rennes, CNRS, ISCR - UMR 6226, F-35000 Rennes, France. [3]Oden Institute for Computational Engineering and Sciences, The University of Texas at Austin, Austin, TX 78712, USA. [4]Department of Physics, The University of Texas at Austin, Austin, TX 78712, USA. ✉email: zachariasmarios@gmail.com; jacky.even@insa-rennes.fr

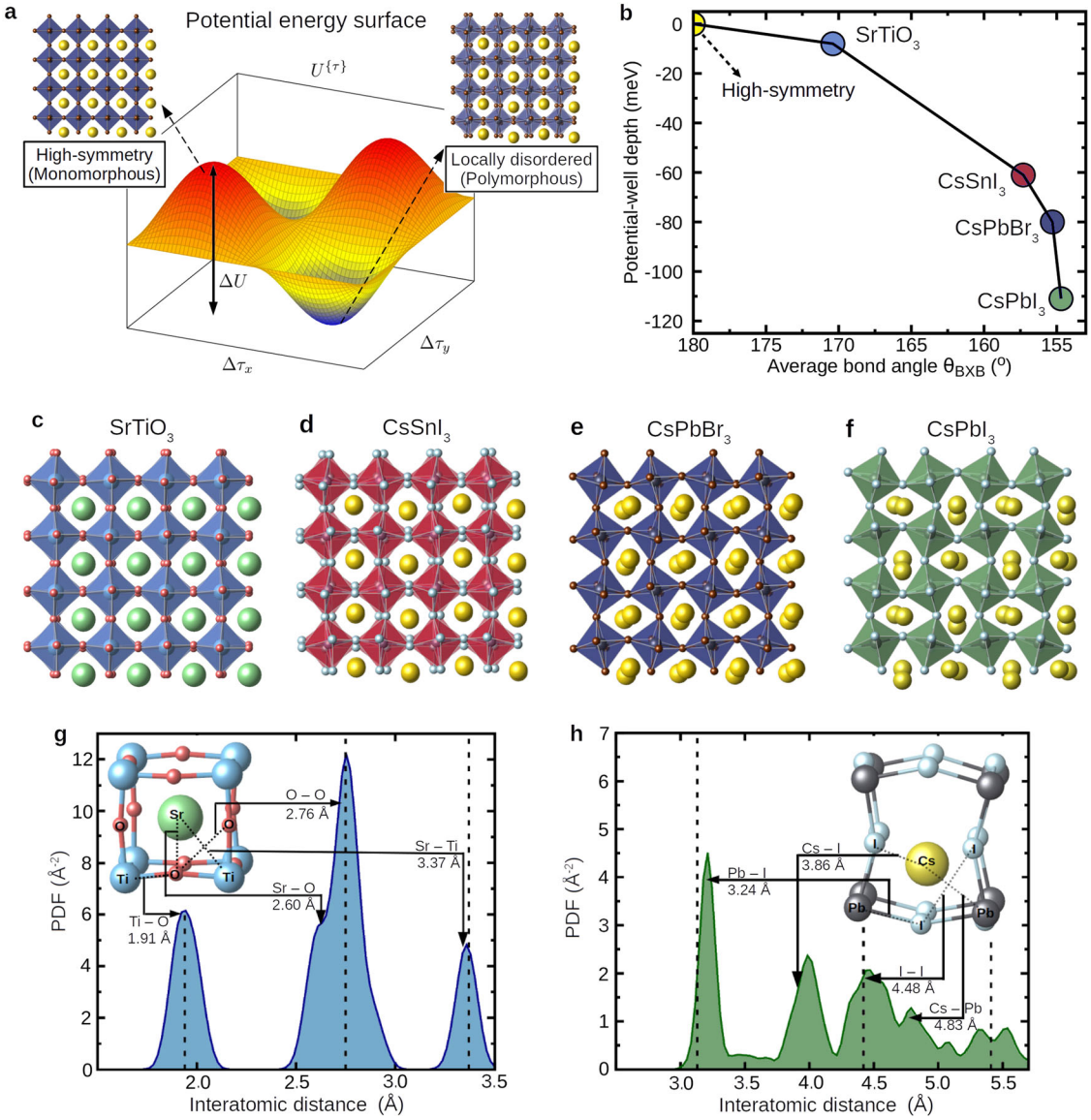

Fig. 1 Locally disordered (polymorphous) structures of cubic perovskites. a Schematic illustration of the potential energy U of cubic perovskites as a function of nuclei displacements $\Delta\tau$. The local maxima or saddle points for $\Delta\tau = 0$ corresponds to the high-symmetry structure with the atoms fixed at their Wyckoff positions. The local minima correspond to locally disordered structures. **b** Potential-well depth (ΔU) calculated for locally disordered cubic $SrTiO_3$, $CsSnI_3$, $CsPbBr_3$, and $CsPbI_3$ using $2\times2\times2$ supercells as a function of the average B-X-B bond angle. **c**–**f** Locally disordered structures of $SrTiO_3$ (**c**), $CsSnI_3$ (**d**), $CsPbBr_3$ (**e**), and $CsPbI_3$ (**f**). More computational details are available in Methods. **g**, **h** Pair distribution function (PDF) of disordered cubic $SrTiO_3$ (**g**) and $CsPbI_3$ (**h**). Vertical dashed lines represent pair distribution functions of the high-symmetry structures.

RESULTS

Lattice dynamics

We start the description of lattice dynamics with the harmonic approximation and take the expansion of a multi-well PES up to second order in atomic displacements to write:

$$U^{\{\tau\}} = U_0 + \frac{1}{2}\sum_{i,i'} C_{i,i'}\,\Delta\tau_i\,\Delta\tau_{i'}. \quad (1)$$

U_0 is the potential energy with the atoms clamped either at their high-symmetry or locally disordered configuration. This statistically disordered initial configuration can be obtained using a similar procedure (see "Methods") to the one described in ref. [14]. Atomic displacements away from a PES extremum are represented by $\Delta\tau_i$ where i is a composite index for the atom, coordinate, and cell. The interatomic force constants (IFCs), defined as $C_{i,i'} = \partial^2 U/\partial\tau_i\partial\tau_{i'}$, are used to compute the phonons of the high-symmetry or locally disordered structures at 0 K, depending on the stationary point at which the second derivatives are evaluated for.

To incorporate anharmonicity in the lattice dynamics we employ the A-SDM that combines the self-consistent phonon theory developed by Hooton[33] and the special displacement method (SDM) developed by Zacharias and Giustino (ZG)[34,35]. In the A-SDM, we fixed the nuclei in a supercell at positions determined by ZG displacements and evaluate the IFCs at temperature T as[32]:

$$C_{i,i'}(T) \simeq \frac{\partial^2 U^{\{\tau^{ZG}\}}}{\partial\tau_i\partial\tau_{i'}}. \quad (2)$$

This procedure is performed iteratively until self-consistency in the phonon spectra is achieved. The merit of the A-SDM is that the ZG nuclei coordinates, $\{\tau^{ZG}\}$, allow to explore automatically an effective temperature-dependent harmonic potential that best

Table 1. Band gaps of high-symmetry and locally disordered perovskites.

	ΔU meV [f.u.]$^{-1}$	$\overline{\theta}_{BXB}$ °	E_g^{srDFT} eV	E_g^{DFT} eV	E_g^{HSE} eV	E_g^{PBE0} eV	$\Delta E_g(T)$ eV	$E_g^{expt.}$ eV
hs-$SrTiO_3$	–	180.0	1.87	1.86	3.09	3.83	−0.17 (300K)	–
d-$SrTiO_3$	−8	170.4	2.11	2.12	3.40	4.15	−0.25 (300K)	3.18
hs-$CsPbBr_3$	–	180.0	1.44	0.23	1.02	1.63	0.30 (430K)	–
d-$CsPbBr_3$	−80	155.3	1.94	0.80	1.68	2.30	0.09 (430K)	2.39
hs-$CsPbI_3$	–	180.0	1.20	0.06	0.58	1.15	0.24 (650K)	–
d-$CsPbI_3$	−111	154.7	1.75	0.62	1.28	1.87	0.06 (650K)	1.78
hs-$CsSnI_3$	–	180.0	0.12	−0.27	0.0	0.0	0.23 (500K)	–
d-$CsSnI_3$	−61	157.3	0.62	0.28	0.73	1.30	0.08 (500K)	1.3

Relative total energy with respect to high-symmetry structure (ΔU), average B-X-B bond angle ($\overline{\theta}_{BXB}$), band gap (E_g), and phonon-induced band gap renormalization ($\Delta E_g(T)$) of high-symmetry (hs) and disordered (d) cubic $SrTiO_3$, $CsPbBr_3$, $CsPbI_3$, and $CsSnI_3$. Calculations of E_g were performed in $2\times2\times2$ supercells using the DFT-PBEsol, HSE, and PBE0 functionals (see "Methods"). $\Delta E_g(T)$ [Eq. (3)] was evaluated using ZG displacements in $4\times4\times4$ supercells by taking as a reference the A-SDM IFCs and nuclei positions obtained for $2\times2\times2$ supercells. Temperatures are such that the cubic phase of each compound is thermodynamically stable. srDFT indicates scalar relativistic DFT calculations; all other reported band gaps include the effect of spin-orbit coupling. Experimental band gaps of cubic $SrTiO_3$, $CsPbBr_3$, $CsPbI_3$, and $CsSnI_3$ are from refs. [48–51], respectively.

captures the solution of the nuclear Schrödinger equation. The anharmonic phonons can then be used to describe the crystal's vibrational properties. The various schemes used to compute phonon dispersions in this work are described in Supplementary Table 2.

Electron–phonon renormalized observables

Here, we take the A-SDM one step beyond and employ the self-consistent $\{\tau^{ZG}\}$ for the nonperturbative evaluation of electron–phonon coupling in anharmonic systems. Following ref. [35], the renormalization of any temperature-dependent property related to the electronic structure can be expressed as:

$$\Delta O(T) = \frac{1}{2}\sum_{\nu}\frac{\partial^2 O^{\{\tau\}}}{\partial x_\nu^2}\sigma_\nu^2 + \mathcal{O}(x_\nu^4), \quad (3)$$

where x_ν represents the normal coordinate of the phonon, σ_ν is the associated mean-square displacement of the atoms, and ν is a composite index for the band and wavevector. The notation $\mathcal{O}(x_\nu^4)$ represents terms of fourth order and higher in x_ν. The ZG displacements derived from the A-SDM define the optimum collection of coordinates within a supercell that allows to compute accurately Eq. (3), describing, at the same time, anharmonicity in the PES. In this work, we focus on electron–phonon renormalized band gaps of tetragonal or cubic perovskites, often described[36] by a harmonic theory introduced by Allen and Heine[37]. In this case, the derivatives $\partial^2 O^{\{\tau\}}/\partial x_\nu^2$ involve linear and second order variations of the PES leading to the Fan–Migdal and Debye–Waller self-energy corrections[38]. Computing the renormalization starting from the locally disordered structure yields different results since (i) electron–phonon self-energy corrections are evaluated for local minima in the PES instead of maxima (c.f. Fig. 1a), (ii) electron wavefunctions are modified, and (iii) phonon frequencies are renormalized.

Potential-well depth and relation to local disorder

The depth of the potential-well is, in principle, equivalent to the potential energy lowering obtained for the ground state structure and provides an indicator of the degree of anharmonicity and static disorder. In Table 1 we report the energy lowering (ΔU) and average B-X-B bond angle ($\overline{\theta}_{BXB}$) calculated for locally disordered cubic $SrTiO_3$, $CsSnI_3$, $CsPbBr_3$, and $CsPbI_3$. Our calculations are in good agreement with data reported in Refs. [14] and [15] (see also Supplementary Table 1). In Fig. 1b, we plot the relationship between local disorder, represented by $\overline{\theta}_{BXB}$, and the potential-well depth. We find that halide perovskites exhibit a considerably higher degree of anharmonicity than $SrTiO_3$ which reflects the larger disorder characterizing their ground state networks (realized schematically in Fig. 1c–f) and PDFs (Fig. 1g, h); this finding is connected to the much softer elastic shear modulus[39,40] as well as the different ionicity and bonding nature of halide perovskites[39,41].

Impact of local disorder on phonons at 0 K

In Fig. 2a, b, we present phonon spectral functions computed for locally disordered $SrTiO_3$ and $CsPbI_3$; for $CsSnI_3$ and $CsPbBr_3$ see Supplementary Fig. 1. We also include phonon dispersions (black) obtained for high-symmetry structures which display large instabilities represented by negative phonon frequencies. Importantly, allowing the systems to explore ground state disorder leads to dynamically stable phonons (color maps). In Fig. 2a, we observe band replicas of the Γ appearing at the R point and vice versa; these features arise from finite size effects and vanish with the supercell size (Supplementary Fig. 2). Local disorder in $SrTiO_3$ also induces a large softening of the acoustic branch along R-M with the frequency at R reaching as low as 2 meV.

Remarkably, polymorphism induces extensive broadening and non-dispersive (flattened) optical bands which are overdamped across the reciprocal space of $CsPbBr_3$, $CsPbI_3$, and $CsSnI_3$ (Fig. 2b–d and Supplementary Fig. 1). Focusing in the frequency region below 4 meV (Fig. 2e), only the acoustic phonons around the Γ-point are clearly identified. This behavior is consistent with experiments performed on lead perovskites[23,42], suggesting that acoustic phonons emerge from a bath of dispersionless optical vibrations (Fig. 2f). Here, we propose a picture of strongly coupled optical vibrations instead of weakly-interacting phonon quasi-particles, since momentum information on phonons is smeared out. In fact, local disorder, which is distinct from thermal disorder arising from vibrational fluctuations[43], is expected to reduce further the phonon correlation lengths and lifetimes of halide perovskites. Due to its low degree of local disorder, this behavior is not adopted by $SrTiO_3$ which exhibits well-defined phonons in the spectral function (Fig. 2a). The extent of vibrational broadening and coupling is also interconnected with the deviation of the PDFs from the archetypal high-symmetry picture (Fig. 1g, h) and lattice softness[40]. Furthermore, local disorder in halide perovskites causes the decrease in energy of optical vibrations, leading to a narrowing of the phonon dispersion and thereby to enhanced phonon bunching (Fig. 2b).

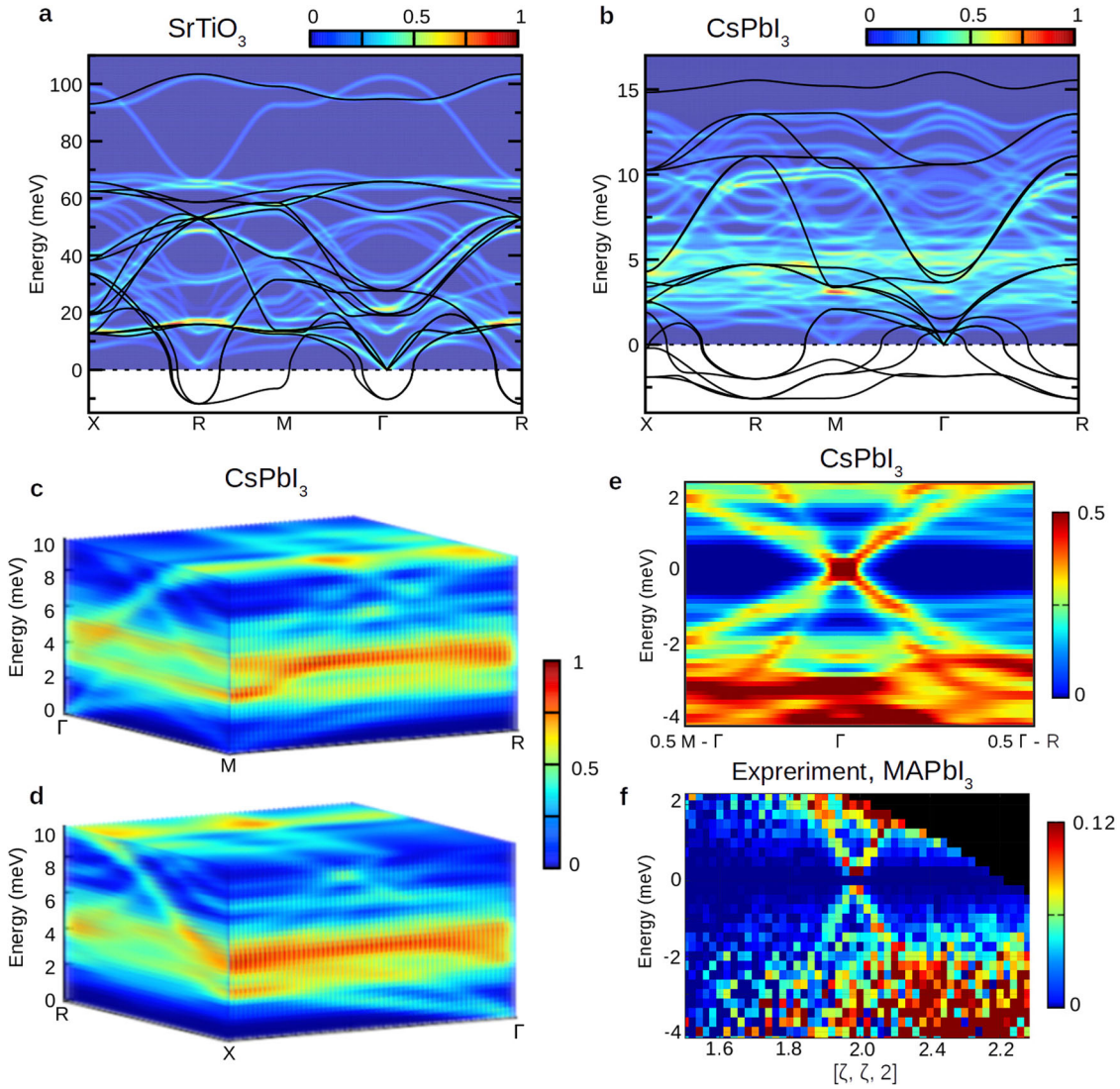

Fig. 2 Vibrational spectra at 0 K of locally disordered oxide and halide perovskites. a, **b** Phonon spectral functions (color maps) of locally disordered cubic $SrTiO_3$ (**a**) and $CsPbI_3$ (**b**) calculated using $2 \times 2 \times 2$ supercells and the phonon unfolding technique (see Methods). Black curves represent phonon dispersions obtained for the high-symmetry structures. All calculations include corrections due to long-range dipole–dipole interactions. **c**, **d** Phonon spectral function of disordered cubic $CsPbI_3$ visualized in 3D. The spectral function spans the momentum plane Γ-X-R-M. **e** Phonon spectral function of disordered cubic $CsPbI_3$ around zone center. The negative region, representing loss of energy in neutron scattering experiments, is obtained as a mirror image of the positive region. **f** Experimental data of methylammonium (MA) lead iodide ($MAPbI_3$) measured by inelastic neutron scattering (positive or negative energy transfers) at room temperature[23].

Figure 3a–c show the phonon spectral functions (color maps) of the three different structural phases of $CsPbBr_3$ calculated using locally disordered networks. In each plot, we report the harmonic phonon dispersions of the monomorphous structures (black lines), the potential well-depth (ΔU), and the total energy difference with respect to the energy of the orthorhombic phase (ΔU_{ORH}). As expected, the level of phonon instabilities in the monomorphous networks are related to the depth of ΔU in each phase. As evidenced by the calculated ΔU_{ORH}, the locally disordered tetragonal and cubic $CsPbBr_3$ lie higher in energy than their orthorhombic analog [Fig. 3d]. It is also apparent that local disorder in the orthorhombic structure has a negligible effect on the system's total energy, yielding identical stable phonons with those obtained for the monomorphous phase. On the contrary, local disorder relatively to the cubic and tetragonal high-symmetry networks is much more prominent, increasing the coupling between individual bands and, hence, suggesting a further decrease in the lattice thermal conductivity of these phases[9].

Temperature-dependent phonon anharmonicity

Figure 4a, b show temperature-dependent phonon dispersions of the high-symmetry (black) $SrTiO_3$ and $CsPbBr_3$ calculated using the A-SDM[32]; for $CsPbI_3$ and $CsSnI_3$ see Supplementary Fig. 3. The phonon spectral functions (color maps) are obtained by combining the atomic positions of locally disordered networks with the IFCs obtained by A-SDM (see also discussion around Supplementary Table 2). It can be seen for $SrTiO_3$ that the spectral function follows closely the A-SDM phonon dispersion. This observation aligns with a picture of non-interacting phonons at low temperatures and it is also related with the minimal level of local disorder in $SrTiO_3$ reported in Table 1. On the contrary, symmetry-breaking in halide perovskites induces the coupling of low-energy optical vibrations and the reduction of their coherence lengths.

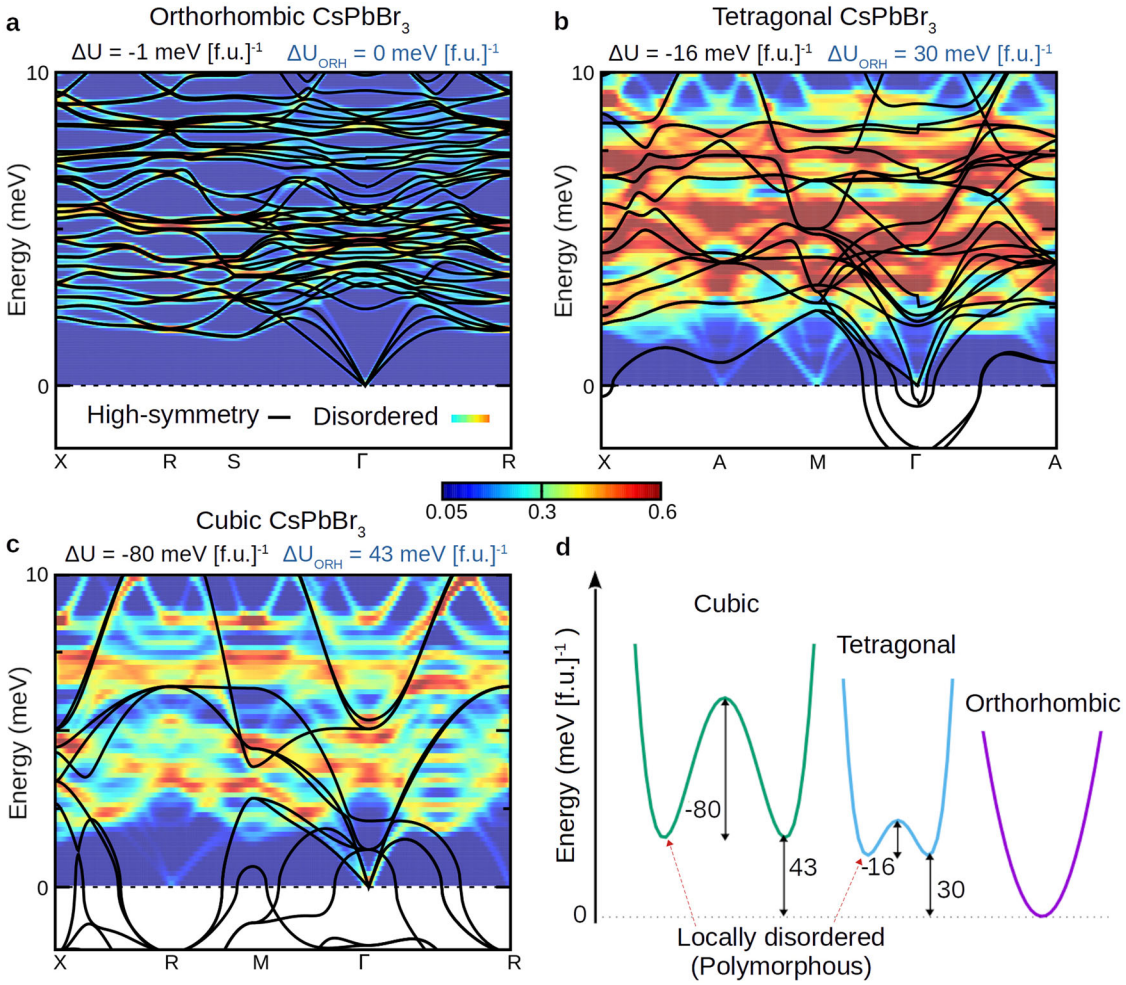

Fig. 3 Vibrational spectra at 0 K of locally disordered halide perovskites for different structural phases. a–c Phonon spectral functions (color maps) of disordered orthorhombic (**a**), tetragonal (**b**), and cubic (**c**) $CsPbBr_3$ calculated using $2\times2\times2$ supercells and the phonon unfolding technique (see "Methods"). ΔU indicates the total energy decrease relative to the corresponding monomorphous structure, and ΔU_{ORH} indicates the total energy increase with respect to the disordered orthorhombic (ORH) phase. All energies are reported in meV per formula unit (f.u., 5 atoms). The harmonic phonon dispersions obtained for the symmetric structures are represented by black curves. Corrections due to dipole-dipole interactions are included. **d** Schematic illustration of the cubic, tetragonal, and orthorhombic PES of $CsPbBr_3$.

Moreover, accounting for temperature-dependent anharmonicity in our calculations via the A-SDM reproduces the thermal vibrational softening along R-M (Fig. 4b and Supplementary Fig. 3), consistent with previous calculations[25,44].

Diffuse scattering

In Fig. 4c–h, we present thermal diffuse scattering maps of $SrTiO_3$ and $CsPbBr_3$ at 300 K and 500 K; for $CsPbI_3$ and $CsSnI_3$ check Supplementary Fig. 4. We find that using the phonons obtained for the disordered networks (i.e spectral function in Fig. 2a) reproduces better the experimental maps[45] of $SrTiO_3$ in (Q_x, Q_y, 1/2) (Fig. 4e) and (Q_x, Q_y, 3/2) (Fig. 4f) reciprocal planes, where $\mathbf{Q} = (Q_x, Q_y, Q_z)$ is the scattering wavevector. Importantly, in the calculated maps we can identify the emergence of phonon-induced scattering peaks at the R-points which correspond to the ultrasoft phonons discussed for Fig. 2a. These features are present in X-ray diffuse scattering measurements of ref. [45] and attributed to dynamic disorder due to antiphase rotations of the octahedra, mimicked by the static distortions present in our disordered network. Note that diffuse scattering at R is absent when the high-symmetry structure with the A-SDM phonons calculated for $2\times2\times2$ supercells are combined (Supplementary Figs. 5 and 6).

At variance with $SrTiO_3$, the scattering maps computed for the high-symmetry $CsPbBr_3$ at 500 K yield better agreement with measurements reported in ref. [25]. To illustrate this we perform calculations of scattering maps in the (Q_x, Q_y, 1/2) plane for two separate frequency ranges (Figs. 4g and 3h) using the A-SDM phonons. Focusing on the scattering induced by ultraslow dynamics (<2.5 meV), the acoustic soft branch along R-M leads to the formation of vertical and horizontal diffuse rods across several Brillouin zones, as observed in measurements for $CsPbBr_3$ (Fig. 4i). We stress that local disorder induces a hardening of the modes along R-M (Supplementary Fig. 1), and thus it prevents the formation of diffuse rods (Supplementary Fig. 7). This comes as no surprise since the disordered network should be regarded as a quasi-static approximation that cannot describe the ultraslow dynamical octahedral tilting[25,26] and, thus, the relaxation of the system between various (deep) minima in the PES. Focusing on the scattering induced by low-energy excitations (2.5–10 meV), we detect broad diffuse rods along M-X (Fig. 4h) which are in close agreement with measurements in the range 2.0–10 meV (Fig. 4j). Now, employing the phonons of the locally disordered network perfectly reproduces the diffuse scattering maps (Supplementary Fig. 4), demonstrating that, unlike the ultraslow octahedra

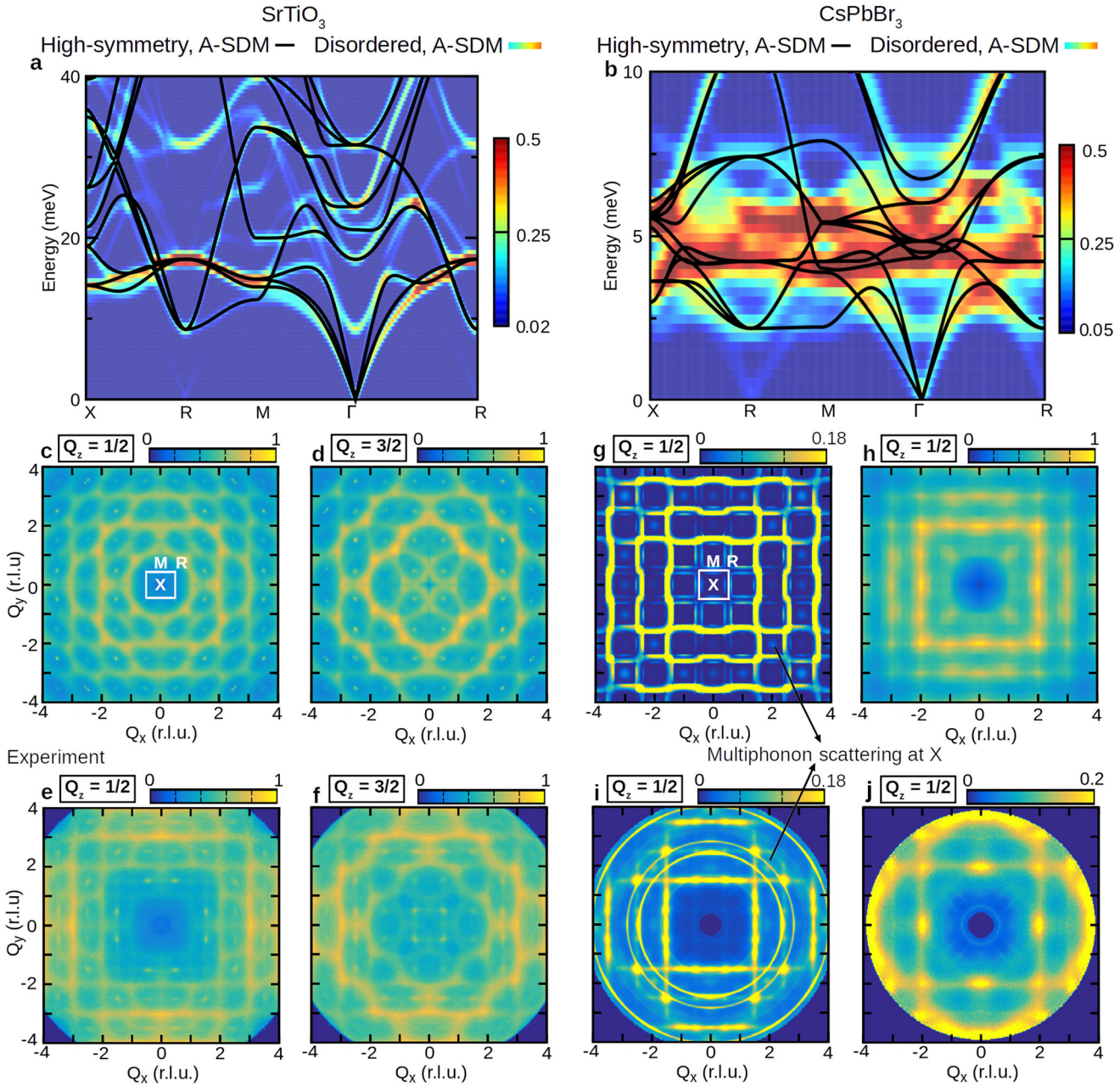

Fig. 4 Temperature-dependent anharmonic phonons of cubic perovskites. a, b Temperature-dependent anharmonic phonons (black lines) of cubic $SrTiO_3$ at 300 K (**a**) and $CsPbBr_3$ at 500 K (**b**) calculated within the A-SDM using $2 \times 2 \times 2$ supercells. Color maps represent phonon spectral functions of the disordered structures. **c**–**f** Computed and measured diffuse scattering maps at 300 K of cubic $SrTiO_3$ in the (Q_x, Q_y, 0) (**c**, **e**) and (Q_x, Q_y, 1/2) (**d**, **f**) reciprocal planes. Calculations are performed using the phonons of the disordered network. X-ray scattering data are from ref. [45]. **g**–**j** Computed and measured diffuse scattering maps at 500 K of cubic $CsPbBr_3$ in (Q_x, Q_y, 1/2) reciprocal plane. Calculations are performed using the A-SDM phonons and high-symmetry network to probe ultraslow (<2.5 meV) (**g**) and low-energy (2.5–10 meV) (**h**) phonon dynamics. Neutron scattering data are from ref. [25] and refer to the energy windows of <2.0 meV (**i**) and 2.0–10 meV (**j**). Diffuse scattering maps are obtained within the Laval–Born–James[81,82] theory (see "Methods"). The scattering wavevector **Q** is expressed in reciprocal lattice units (r.l.u.). Various schemes used to compute phonons and diffuse scattering are discussed in Supplementary Table 2.

relaxations (<2.5 meV), the low-energy vibrations (2.5–10 meV) are captured correctly.

Interestingly, in Fig. 4g and Supplementary Fig. 4, we can identify low intensity multiphonon scattering signatures at the X-points arising from the combined momenta of two phonons along M-R. These fine structures are present in neutron scattering maps of $CsPbBr_3$ (Fig. 4i), but not interpreted before. Our findings here suggest that low-energy multiphonon excitations are another source of manifestation of anharmonicity in halide perovskites, emerging from highly anharmonic zone-edged modes.

Effect of disorder on anharmonic electron–phonon coupling

Figure 5a, b compare the electron spectral functions of locally disordered cubic $SrTiO_3$ and $CsPbI_3$ (color maps) with the band structures of their high-symmetry counterparts (black); for $CsSnI_3$

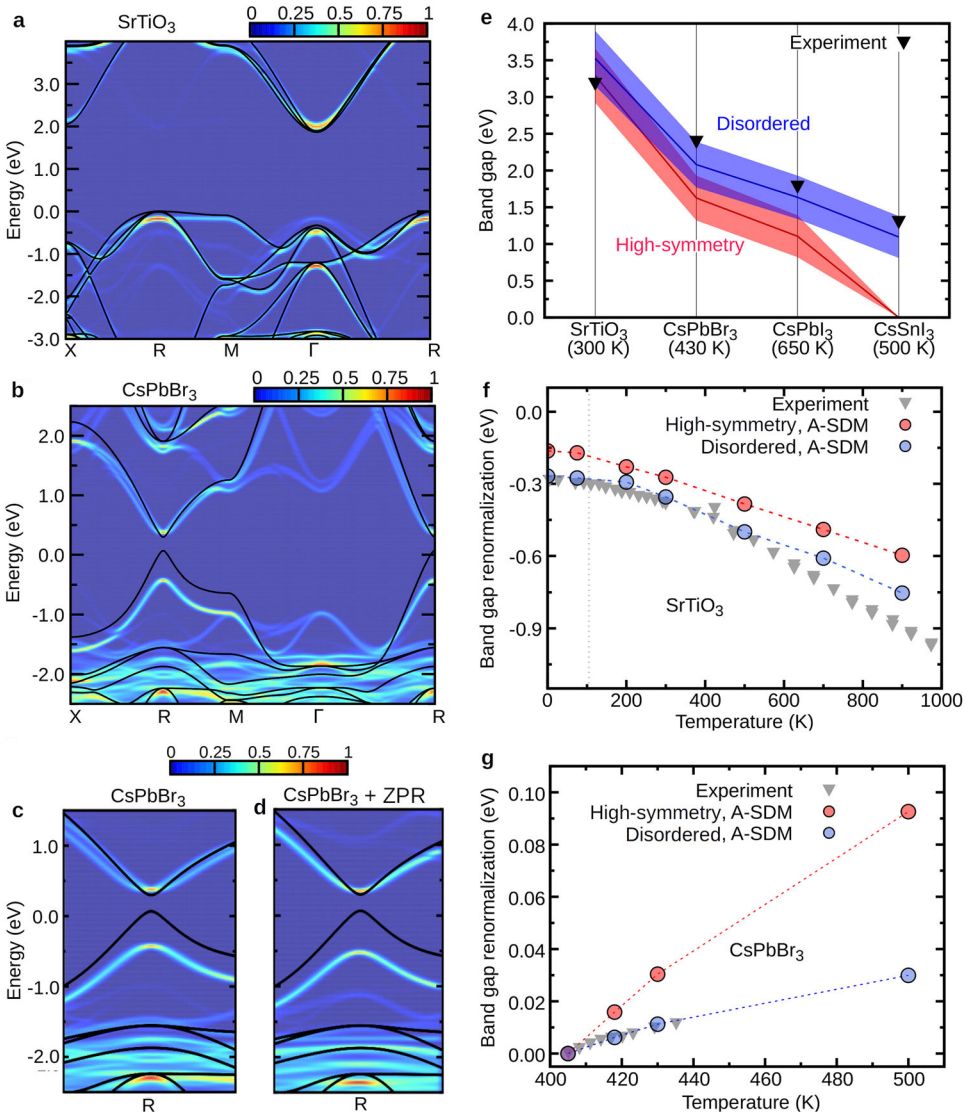

Fig. 5 Electron–phonon renormalized band gaps of cubic perovskites. a, **b** Fully-relativistic electron spectral functions (color maps) of disordered cubic $SrTiO_3$ (**a**) and $CsPbI_3$ (**b**) calculated using $2 \times 2 \times 2$ supercells and the band unfolding technique[35]. Black curves represent the band structures of the high-symmetry networks. **c** As in (**b**) but now focusing around the band edges at R. **d** As in (**c**) but now the effect of electron–phonon coupling at 0 K [i.e. the ZPR] via the A-SDM is included. **e** HSE and PBE0 band gaps of high-symmetry and disordered cubic perovskites including the effect of SOC and electron–phonon coupling. Lines represent the average of HSE and PBE0 band gaps and the shaded areas define the uncertainty. Experimental gaps (black) of $SrTiO_3$, $CsPbBr_3$, $CsPbI_3$, and $CsSnI_3$ are from refs. [48–51]. **f**, **g** Phonon-induced band gap renormalization of high-symmetry (red) and disordered (blue) cubic $SrTiO_3$ (**f**) and $CsPbBr_3$ (**g**) as a function of temperature calculated using ZG displacements for $6 \times 6 \times 6$ and $4 \times 4 \times 4$ supercells, respectively. The data below the phase transition temperature (~105 K) of $SrTiO_3$ are obtained using the tetragonal structure and ZG displacements for $6 \times 4 \times 4$ supercells. ZG displacements were generated using anharmonic A-SDM IFCs and accounting for thermal lattice expansion. For $CsPbBr_3$ the effect of SOC is included and the renormalization is determined with respect to $T = 405$ K. Optical spectroscopy data (gray) for $SrTiO_3$ and $CsPbBr_3$ are from refs. [48,49]. Except for (**e**) all calculations are performed within DFT-PBEsol.

and $CsPbBr_3$ check Supplementary Fig. 8. The effect of symmetry-breaking domains on the electronic structure can be understood intuitively by inspection of the PDFs (Fig. 1g, h). It turns out that local disorder induces slight changes in the electronic structure of $SrTiO_3$ with the main impact being on the band edges at Γ and R points (Fig. 5a). In particular, symmetry lowering induces a band gap opening of 0.24 eV which is in agreement with the value reported in ref. [15].

Local disorder causes distinct changes on the electronic structure of cubic halide perovskites (Fig. 5b and Supplementary Fig. 8). Those are large band gap openings, band dispersion renormalization, and band broadening. The quantitative comparison between the band gaps calculated for the high-symmetry and disordered halide perovskites is provided in Table 1. Our calculations reveal a band gap enhancement due to local disorder of more than 0.50 eV for cubic $CsPbBr_3$, $CsPbI_3$, and $CsSnI_3$, similarly to previous calculations[14]. Owing to a higher degree of local disorder, represented by $\overline{\theta}_{BXB}$ in Table 1, halide perovskites exhibit a larger band gap opening than $SrTiO_3$. Interestingly, this observation suggests an indirect relationship between anharmonicity and the band gap in perovskite systems. In fact, the connection between $\overline{\theta}_{BXB}$ with the band gap is related to the changes in the overlap between the metal and halogen states[41]. Moreover, our calculations show that local disorder in the tetragonal and orthorhombic phases of $CsPbBr_3$ yields band gap enhancements of 0.17 and 0.001 eV. These values are much lower than the one obtained for the cubic phase (0.57 eV), in line

with the potential well-depth of each phase (Fig. 3d). Our values for the Pb-based compounds in Table 1 show that spin-orbit coupling (SOC) induces a giant gap closing of 1.1–1.2 eV, in agreement with ref. [46]. We find that SOC has also a strong influence on the effective mass enhancement due to local disorder (Supplementary Table 3). For instance, excluding SOC, local disorder leads to electron and hole mass enhancements λ (see "Methods") between 0.4–1.2. When SOC is taken into account, the disordered networks yield λ of 1.3–2.3 for $CsPbBr_3$ and 3.3–4.7 for $CsPbI_3$. We stress that the calculated effective masses of disordered $CsPbBr_3$ and $CsPbI_3$, ranging between 0.13–0.20, compare well with 0.114 and 0.126 measured from inter-Landau level transitions in $CsPbI_3$ and $CsPbBr_3$, respectively[47].

The impact of local disorder is clearly manifested in the electronic structure of $CsSnI_3$ (Supplementary Fig. 8). The fully relativistic band structure of high-symmetry $CsSnI_3$ exhibits an artifact in the conduction band minimum, resulting from the exchange of orbital character between the band edges. This suggests a metallic-like behavior for $CsSnI_3$ (hence the value -0.27 eV in Table 1) and leads to unphysical negative electron effective masses at the R-point. Instead, accounting for local disorder recovers the standard picture of a parabolic conduction band minimum with positive effective masses of 0.08 and a direct gap of 0.28 eV at the R-point.

The fully relativistic DFT band gaps of disordered perovskites still largely underestimate the experimental values[48–51], reported in Table 1, by more than 1 eV, due to the DFT semi-local description of correlation effects. As shown in Table 1, this discrepancy is significantly alleviated when self-energy corrections through the HSE and PBE0 hybrid functionals are accounted for.

In Fig. 5c, d, we compare the electronic structure around the band extrema of disordered $CsPbBr_3$ without and with the effect of phonon-induced zero-point renormalization (ZPR)[35]. Electron–phonon interactions, incorporated by ZG displacements in $2\times2\times2$ supercells, induce a band gap opening, yielding a ZPR of 29 meV. Increasing the supercell size to $4\times4\times4$ reverses the sign of the ZPR and yields a band gap decrease of 35 meV. We also comment that combining disorder with ZG displacements does not lead to an artificial Rashba–Dresselhaus splitting of the doubly degenerate band extrema, reflecting that perovskite crystals should maintain centrosymmetricity at thermal equilibrium[52].

Table 1 also reports the phonon-induced band gap renormalization, $\Delta E_g(T)$, of cubic $SrTiO_3$, $CsPbBr_3$, $CsPbI_3$, and $CsSnI_3$ at 300, 430, 650, and 500 K, respectively, using $4\times4\times4$ ZG supercells. It turns out that electron–phonon interactions at finite temperatures result in the closure of the band gap in $SrTiO_3$, whereas in halide perovskites, electron–phonon interactions cause the opening of the band gap. Accounting for local disorder in all compounds reduces $\Delta E_g(T)$ by 80–210 meV. This is related to the different potential experienced by electrons in the disordered network, affecting the electron–phonon matrix elements (see also discussion around Eq. (3)). Interestingly, for halide perovskites, we observe an almost linear correlation [33 meV/(°)] between the reduction in $\Delta E_g(T)$ due to disorder and the decrease in $\overline{\theta}_{BXB}$.

Figure 5e shows that experimental values lie within the range of our electron–phonon corrected HSE and PBE0 band gaps for all disordered compounds. In fact, by adding $\Delta E_g(T)$ to the average PBE0/HSE gap yields 3.53, 2.08, 1.64, and 1.10 eV for cubic $SrTiO_3$, $CsPbBr_3$, $CsPbI_3$, and $CsSnI_3$, respectively, in good agreement with experiments. Our findings here suggest that accurate electronic structure calculations of cubic perovskites require the combined corrections due to local disorder, SOC, functionals beyond DFT[53], and electron–phonon coupling.

In Fig. 5f, g, we show the temperature dependence of the band gap renormalization evaluated for the high-symmetry (red) and locally disordered (blue) cubic $SrTiO_3$ and $CsPbBr_3$ using the A-SDM. Our calculations for high-symmetry $SrTiO_3$ underestimate experimental data (black) from ref. [48]. This underestimation is reduced when the disordered network is employed. In fact, electron–phonon coupling is strongly modified inducing a correction to the band gap closing of ~30%. This finding together with the computed diffuse scattering patterns further support the presence of local disorder in cubic $SrTiO_3$. As seen in Fig. 5g, using the disordered $CsPbBr_3$ also provides an accurate description of the band gap renormalization, explaining the low variation of the experimental data with temperature[50]. Our analysis (see "Methods") yields that the low-energy anharmonic optical vibrations dominate electron–phonon coupling in locally disordered halide perovskites, contributing 88% to the band gap renormalization, but strongly departing from the simplified picture of a Fröhlich interaction related to harmonic modes. This is consistent with photoluminescence spectra measurements of halide perovskite nanocrystals, which suggest a dominant (negligible) contribution of low-energy optical vibrations (acoustic phonons) to exciton–phonon coupling[54]. The band gap renormalization calculated using the high-symmetry structure is consistently 300% larger than experiment, fact that further casts doubt on the use of a fully ordered network in first-principles calculations of cubic halide perovskites. The remarkable success of the cubic polymorphs in describing electron–phonon coupling is explained by inspecting the electron lifetimes in halide perovskites (~4–6 fs)[55,56] which are much smaller relatively to the period of atomic vibrations (>200 fs). Hence, anharmonic structural fluctuations look essentially static to the electrons which follow the nuclei in their most probable ground state configuration. We remark that polaronic effects on the band gap renormalization are not included in our calculations. Although it is now possible to combine ab initio polaron distortions[57] with the A-SDM, such calculations are rather challenging and beyond the scope of this work. We also note that corrections to the band gap renormalization coming from hybrid functionals are less than 1 meV (see "Methods").

In Fig. 6, we show the band gap variation of $CsPbBr_3$ with temperature calculated within A-SDM using the cubic and

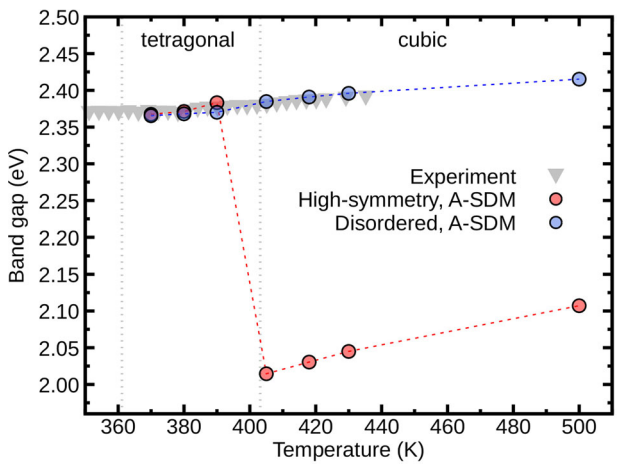

Fig. 6 Temperature-dependent band gaps of $CsPbBr_3$ across different phases. Band gap of $CsPbBr_3$ as a function of temperature calculated for the high-symmetry (red) and locally disordered (blue) networks in the tetragonal and cubic phases using the A-SDM. ZG supercells of size $4\times4\times4$ and $4\times2\times4$, containing 320 atoms each, were used for the cubic and tetragonal phases, respectively. ZG displacements for the disordered networks were generated by taking as a reference the disordered nuclei positions obtained for $2\times2\times2$ supercells. DFT-PBEsol data for the high-symmetry and disordered networks are shifted by 1.50 and 1.42 eV, close to the PBE0 corrections, to match the experimental band gaps at 370 K. The dashed gray lines indicate the phase transition temperatures at 361 K and 403 K. Band gap renormalization due to thermal lattice expansion and SOC are accounted for. Experimental data (gray) are from ref. [49].

tetragonal phases. Remarkably, accounting for local disorder in our anharmonic electron–phonon coupling calculations (blue) yields good agreement with experiment (gray) and captures the smooth variation of the measured band gap around the continuous phase transition temperature at 403 K. Instead, using the high-symmetry structures of the tetragonal and cubic phases (red), the band gap exhibits a spurious abrupt drop of ~0.4 eV, primarily caused by the enforced alignment of the octahedra in the cubic phase. A similar issue for the temperature-dependent band gaps computed for the high-symmetry $CsPbI_3$ networks has been observed previously[58]. The continuous change of the band gap from the disordered cubic to the disordered tetragonal phase, achieved here, is consistent with a second-order displacive phase transition. We stress that for all computed values we account for the same PBE0 corrections to the band gap; that is we apply an identical shift to the temperature-dependent band gaps of both the tetragonal and cubic phases. In our calculations for the disordered structures we combined A-SDM temperature-dependent IFCs with the disordered networks to generate ZG displacements; examples of the resulting phonon spectral functions are shown in Supplementary Fig. 17. Notably, using 0 K ground state phonons obtained for the disordered structures (Fig. 3b, c) yields a similar level of agreement (Supplementary Fig. 18). This demonstrates, essentially, that the vibrational dynamics computed for the locally disordered networks is a reasonable approximation to describe anharmonic electron–phonon effects originating from low-energy optical vibrations.

DISCUSSION

Taken all together, our work provides insights on the lattice dynamics and electron–phonon couplings in oxide and halide perovskites. Given the agreement with measurements of the vibrational-induced band gap renormalization of $SrTiO_3$ and $CsPbBr_3$, we expect our approach to be widely used for addressing open challenges related to important technological applications of halide and oxide perovskites, such as solar cells, light emitting diodes, and thermoelectric devices, as well as elucidating their unexplored ultrafast spectroscopic properties[59]. Our results demonstrate that $SrTiO_3$ is fully compatible with a static disordered network, while $CsPbBr_3$ is better described within a quasi-static picture that captures correctly optical vibrations but not effects arising from ultraslow relaxational rotations of the BX_3 octahedra. Our findings also confirm that vibrational dynamics in halide perovskites deviate from a textbook noninteracting phonon dispersion; a picture of strongly coupled vibrations should be considered as a precursor to future calculations of perovskites' peculiar transport properties[10,11]. In the context of electron–phonon coupling, the description of tetragonal or cubic perovskites with a locally disordered network constitutes the best possible approximation since (i) electron coupling to anharmonic optical vibrations is predominant, (ii) dynamical structural fluctuations look essentially static to the short-lived electrons, and (iii) electrons mostly see the nuclei as fixed in their disordered ground state. This latter point also allows to explain the continuous variation of the band gap around phase transitions in halide perovskites, reflecting the subtle rearrangement of atomic positions between different phases. Some of the important physics of halide perovskites uncovered here are intrinsically related to their extraordinary lattice softness[40], and, thus, their remarkable ability to sustain a high degree of disorder. At a fundamental level, our study proposes a radically different way of conceptualize the lattice dynamics in perovskites and sets up a universal framework for accurate simulations of their carrier mobilities, conductivities, excitonic spectra, non-equilibrium dynamics, and polaron physics[60–62].

METHODS

Electronic structure calculations

Electronic structure calculations for $SrTiO_3$, $CsPbBr_3$, $CsPbI_3$, and $CsSnI_3$ were performed within density functional theory using plane waves basis sets as implemented in `Quantum Espresso` (QE)[63,64]. We employed a kinetic energy cutoff of 120 Ry, the Perdew–Burke–Ernzerhof exchange–correlation functional revised for solids (PBEsol)[65], and optimized norm-conserving Vanderbilt pseudopotentials from the PseudoDojo library[66,67]. To account for the effect of SOC on the electronic structures we replaced scalar relativistic with fully relativistic pseudopotentials. The uniform sampling of the Brillouin zone of the cubic $1\times1\times1$, $2\times2\times2$, $4\times4\times4$, and $6\times6\times6$ supercells was performed using $6\times6\times6$, $3\times3\times3$, $1\times1\times1$, and $1\times1\times1$ **k**-grids, respectively. The only exception is that for $4\times4\times4$ supercells of $SrTiO_3$ we employed a $2\times2\times2$ **k**-grid. Furthermore, for $6\times6\times6$ supercells we reduced the kinetic energy cutoff to 100 Ry. Initial calculations of the monomorphous structures were performed in the unit cells of the cubic (5 atoms), tetragonal (10 atoms), and orthorhombic (20 atoms) perovskite compounds with the nuclei clamped at their Wyckoff positions (space groups: $Pm\bar{3}m$ for all cubic perovskites, $I4/mcm$ for tetragonal $SrTiO_3$, $P4/mbm$ for tetragonal $CsPbBr_3$, and $Pbnm$ for orthorhombic $CsPbBr_3$). The lattice constants of cubic $SrTiO_3$, $CsPbBr_3$, $CsPbI_3$, and $CsSnI_3$ were fixed to the DFT-PBEsol optimized values of 3.889, 5.874, 6.251, and 6.141 Å, respectively. The lattice constants of the tetragonal and orthorhombic $CsPbBr_3$ were also fixed to the DFT-PBEsol optimized values of ($a=b=$ 5.734, $c=5.963$ Å) and ($a=7.971$, $b=8.397$, and $c=11.640$ Å). The lattice constants of the tetragonal $SrTiO_3$ were fixed to the experimental lattice constants[68] of ($a=b=3.896$ and $c=3.900$ Å) since were found to yield better phonon frequency renormalizations due to anharmonic effects at finite temperatures[32]. The eigenmodes and eigenfrequencies at each phonon wavevector **q** were obtained by evaluating the IFCs and corresponding dynamical matrices via the frozen-phonon method[69,70]. Corrections on the phonon dispersions due to long-range dipole–dipole interactions, which vary depending on the degree of static-disorder[32], were included via the linear response approach described in ref. [71].

Electron spectral functions of the disordered cubic structures were calculated using the electron band structure unfolding technique as implemented in the `EPW/ZG` code[35,57]. We ran calculations with and without SOC (see Supplementary Figs. 8 and 9) and sampled the Brillouin zone with 417 equally-spaced **k**-points along the X-R-M-Γ-R path. We remark that when SOC is excluded, local distortions in a $2\times2\times2$ supercell of $SrTiO_3$ lead to an artificial degeneracy splitting of 40 and 60 meV of the triply degenerate valence band top and conduction band bottom, respectively. Interestingly, our calculations for a $4\times4\times4$ supercell show that the splitting in the valence band top is eliminated, while in the conduction band bottom is maintained. This result is consistent with a disordered network that macroscopically might reflect some of the crystal's symmetries, although local deformations are present. Inclusion of fully relativistic effects in our calculations for $SrTiO_3$ induces a small band gap change and spin-orbit splitting of the band edges, as shown in Table 1 and Supplementary Fig. 9. Our fully relativistic calculations for the band gaps of the high-symmetry and locally disordered tetragonal $CsPbBr_3$ within DFT-PBEsol yield 0.69 and 0.86 eV, respectively. Ignoring SOC effects our calculations determine 1.65 and 1.83 eV for the high-symmetry and locally disordered tetragonal $CsPbBr_3$. Data calculated for all cubic compounds are provided in Table 1.

To extract effective masses m^* at the band edges we performed parabolic fits to the electron band structure and spectral functions along the specified directions reported in Supplementary Table 3. The mass enhancement due to disorder, λ, was obtained from $m_d^* = (1+\lambda)\, m_{hs}^*$, where m_d^* and m_{hs}^* are the disordered and high-

symmetry structure's effective masses. We note that at the proximity of the band edges, the electron spectral functions give well-defined bands that do not suffer from band broadening.

All calculations employing the Perdew–Burke–Ernzerhof (PBE0)[72] and Heyd–Scuseria–Ernzerhof (HSE06)[73] hybrid functionals were performed using the code VASP[74]. SOC was taken into account, and a 300 eV cut-off energy was set for the projector-augmented wave[75]. For the high-symmetry and $2\times2\times2$ supercell disordered structures we employed Γ-centered **k**-grids of $4\times4\times4$ and $2\times2\times2$, respectively. The HSE06 (PBE0) band gaps with SOC of the high-symmetry and locally disordered tetragonal $CsPbBr_3$ are found to be 1.20 eV (1.80 eV) and 1.69 eV (2.31 eV), respectively. The corresponding values for all cubic compounds are reported in Table 1.

The locally disordered (polymorphous) network

To explore, initially, the locally disordered network of cubic $SrTiO_3$ we applied three different initial sets of displacements on the atoms of the high-symmetry structure in a $2\times2\times2$ supercell. Those are: (i) ZG displacements along all phonon modes populated at $T=0$ K, (ii) ZG displacements along the soft modes populated at $T=0$ K and, (iii) random displacements smaller than 0.1 Å applied to all atomic coordinates. We note that ZG displacements along imaginary soft modes were generated by switching their frequencies to real. Each case was followed by a DFT-PBEsol relaxation of the nuclei. Although three different ground state disordered geometries were realized, a consistent energy lowering of 8 meV $[f.u.]^{-1}$ relative to the ordered structure was obtained. Starting from random initial displacements in a $4\times4\times4$ supercell, the relaxation yields the same energy lowering of 8 meV $[f.u.]^{-1}$ in good agreement with the value of 12 meV $[f.u.]^{-1}$ reported in ref. [15]. In Supplementary Fig. 10, we demonstrate that the three disordered structures give identical PDFs. In Supplementary Table 1, we show that accounting for ground state symmetry-breaking domains in $4\times4\times4$ supercells yields similar band gap openings with $2\times2\times2$ supercells.

Having demonstrated the equivalence of the three disordered structures, which give the same ground state energy and PDF, now we comment on the best choice of initial displacements [see (i)–(iii) above]. The most computationally inefficient choice is the use of ZG displacements along all phonon modes, bringing the initial configuration well away from its ground state. Instead, the relaxation converges much faster when ZG displacements along the soft modes are used which reproduce the tilting of the octahedra and thus bring the structure closer to the bottom of the potential well[76]. Using random nudges, the efficiency of generating the ground state network might vary depending on the system and the amplitude of the initial displacement. Therefore, for generating all locally disordered structures, we chose to apply special displacements[34,35] along the soft modes (computed for the high-symmetry structures) which is the most practical and systematic way to achieve ground state optimization.

The locally disordered (polymorphous) networks of cubic, tetragonal, and orthorhombic phases were explored (unless specified otherwise) by employing $2\times2\times2$ supercells containing 40, 80, and 160 atoms, respectively. To check whether the locally disordered cubic geometries exhibit any residual symmetries, we perform a symmetry analysis with `pymatgen`[77] using a tolerance factor of 0.0001 Å; we confirm that none of the locally disordered cubic structures maintain residual symmetries.

Special displacement method

ZG displacements were generated via the special displacement method[34,35] (SDM) as implemented in the `EPW/ZG` code. We used phonons at **q**-points commensurate with the supercell size and applied a smooth phase evolution of the phonon eigenvectors in reciprocal space.

Anharmonicity in our calculations was included via the A-SDM using $2\times2\times2$ supercells as described in ref. [32]. Self-consistency in the phonon spectra of each system was achieved using only 3-4 iterations by means of a linear mixing scheme. To incorporate the effect of anharmonicity in the phonon-induced band gap renormalization, we generated ZG displacements in $4\times4\times4$ (all cubic perovskites), $6\times6\times6$ (cubic $SrTiO_3$), $4\times2\times4$ (tetragonal $CsPbBr_3$), and $6\times4\times4$ (tetragonal $SrTiO_3$) supercells employing the IFCs obtained by A-SDM. In all calculations of temperature-dependent band gaps reported in Fig. 5f, g, we allowed the lattice to expand according to the measured expansion coefficient[51,78]. Symmetry breaking in ZG configurations led to an artificial degeneracy splitting of the band edges of cubic and tetragonal $SrTiO_3$. In this case, the band gap renormalization of $SrTiO_3$ at each temperature was evaluated by averaging the energy change of all states participating in the formation of the band edges within an energy window of 20 meV. To ensure high accuracy and limit the errors arising from artificial degeneracy splitting, we also took the average over the band gap renormalization obtained for four different ZG configurations. In Supplementary Fig. 11, we show that the band gap renormalization of cubic $SrTiO_3$ remains nearly the same when SDM is combined with 0 K ground state phonons obtained for the disordered structure.

To identify the contribution of ultraslow acoustic ($E<2.5$ meV) and low-energy optical vibrations ($3.65<E<10$ meV) to the band gap renormalization of $CsPbBr_3$, we applied ZG displacements on the nuclei along only the phonons lying within the associated energy windows. We note that using phonons with energies $E>2.5$ meV and $2.5<E<10$ meV we obtain a similar band gap renormalization (within 25 meV) which demonstrates, essentially, that high-energy optical vibrations ($E>10$ meV) do not play an important role in the electron–phonon gap renormalization of halide perovskites.

All A-SDM calculations for determining the phonon-induced band gap renormalization were performed at the DFT-PBEsol level. Corrections to the band gap renormalization arising from hybrid functionals were found to be negligible. In particular, our calculations in $2\times2\times2$ ZG supercells of disordered $CsPbBr_3$ yield a ZPR of 29.4, 29.0, and 29.9 meV for DFT-PBEsol, HSE, and PBE0 functionals, respectively.

Phonon unfolding

For systems undergoing static symmetry breaking due to lattice distortion coming, e.g., from defects, atomic disorder, or a charge density wave, a supercell is required to compute the phonons. In this case, the crystal's symmetry operations (translations and rotations) are no longer applicable and all atoms in the supercell need to be displaced for calculating the dynamical matrix and, hence, the renormalized phonon frequencies $\omega_{\mathbf{Q}\mu}$, where **Q** and μ are the phonon wavevector and band indices. To illustrate the effect of lattice distortion in the phonons, a common practise is to employ phonon unfolding and evaluate the momentum-resolved spectral function given by[79]:

$$A_{\mathbf{q}}(\omega)=\sum_{\mathbf{Q}\mu}P_{\mathbf{Q}\mu,\mathbf{q}}\,\delta(\omega-\omega_{\mathbf{Q}\mu}). \tag{4}$$

Here **q** denotes a wavevector in the Brillouin zone of the unit cell and $P_{\mathbf{Q}\mu,\mathbf{q}}$ represents the spectral weights which are evaluated in the spectral representation of the single-particle Green's function as[80]:

$$P_{\mathbf{Q}\mu,\mathbf{q}}=\frac{1}{N_{\mathbf{g}}}\frac{\Omega}{\tilde{\Omega}}\sum_{aj}\Big|\sum_{\kappa}\tilde{e}_{a\kappa,\mu}(\mathbf{q})e^{i(\mathbf{q}+\mathbf{g}_j)\cdot\tilde{\boldsymbol{\tau}}_\kappa}\Big|^2, \tag{5}$$

where j is an index for the reciprocal lattice vectors **g** of the unit cell Brillouin zone, a denotes a Cartesian direction, and κ is the atom index. The symbol ~ indicates quantities calculated using the disordered structure. $N_{\mathbf{g}}$ acts as a normalization factor representing the total number of reciprocal lattice vectors entering the summation. The spectral weight can be understood, essentially, as

the projection of the phonon eigenvector $\tilde{e}_{\alpha\kappa,\mu}(\mathbf{Q})$ on the phonon eigenvectors $e_{\alpha\kappa,\nu}(\mathbf{q})$ computed in the unit cell, given that $\mathbf{Q}$ unfolds into $\mathbf{q}$ via $\mathbf{Q} = \mathbf{q} + \mathbf{g}_j - \mathbf{G}$, where $\mathbf{G}$ is a reciprocal lattice vector of the distorted structure.

To generate vibrational spectral functions we employed Eq. (5) and 417, 382, and 399 equally-spaced $\mathbf{q}$-points along the X-R-M-Γ-R (cubic), X-A-M-Γ-A (tetragonal), and X-R-S-Γ-R (orthorhombic) paths. Convergence of the spectral weights was ensured by using a $10 \times 10 \times 10$ $\mathbf{g}$-grid of reciprocal lattice vectors. In Supplementary Figs. 12 and 13, we demonstrate our implementation of phonon unfolding by comparing phonon spectral functions computed for $2 \times 2 \times 2$ and $4 \times 4 \times 4$ supercells of $SrTiO_3$. Our implementation of phonon unfolding is available in the `EPW/ZG` tree. In Supplementary Fig. 14, we also show that the vibrational spectrum of $CsPbBr_3$ remains almost identical when two different ground state disordered geometries are considered.

We note that overdamped unfolded phonon spectra of halide perovskites has also been revealed by analysis of velocity autocorrelation functions obtained by molecular dynamics simulations[43].

Diffuse scattering

All-phonon diffuse scattering maps were calculated within the Laval-Born-James (LBJ) theory using `disca.x` of the `EPW/ZG` code[81,82]. The merit of the LBJ theory is that inelastic scattering arising from one-phonon and multiphonon processes is accounted for on the same basis. The Debye-Waller and phononic factors entering LBJ theory [Eq. (1) of ref. [81]] were evaluated for a $16 \times 16 \times 16$ $\mathbf{q}$-grid. The phonon eigenmodes and frequencies were obtained by means of Fourier interpolation of the dynamical matrices computed for $2 \times 2 \times 2$ supercells using either the A-SDM or the disordered network. A $16 \times 16 \times 1$ uniform $\mathbf{Q}$-grid (scattering wavevectors) per Brillouin zone was used to calculate the phonon-induced scattering intensity in the reciprocal lattice planes perpendicular to one Cartesian axis. The atomic scattering amplitudes were determined as a sum of Gaussians with the parameters taken from ref. [83]. The diffuse scattering maps of $CsPbBr_3$ for ultraslow acoustic and low-energy phonon dynamics were determined by excluding the modes outside the associated energy windows. In addition to the scattering maps of cubic $SrTiO_3$ presented in Fig. 4, we also calculated diffuse scattering in the $(Q_x, Q_y, 0)$ and $(Q_x, Q_y, 1)$ planes and found qualitative agreement with measurements of ref. [45] (Supplementary Figs. 5 and 6). In Supplementary Figs. 15 and 16, we show the decomposition of the all-phonon scattering in the $(Q_x, Q_y, 0)$ planes of cubic $SrTiO_3$ and $CsPbBr_3$ into one-phonon and multiphonon processes for a large range of scattering wavevectors.

DATA AVAILABILITY

The calculations (input and output files) employed for this study are available via the NOMAD archive [https://doi.org/10.17172/NOMAD/2023.07.11-1 for anharmonic electron–phonon coupling calculations and https://doi.org/10.17172/NOMAD/2023.05.13-1 for anharmonic phonon calculations], or upon request from the corresponding author.

CODE AVAILABILITY

QUANTUM ESPRESSO is available under GNU General Public Licence from the QUANTUM ESPRESSO web site (https://www.quantum-espresso.org/). The ZG module of EPW employed for the treatment of local disorder, anharmonicity, and generation of anharmonic self-consistent special displacements is also available at GitLab (https://gitlab.com/epw-code/q-e/tree/ZG).

Received: 23 February 2023; Accepted: 19 July 2023;
Published online: 24 August 2023

REFERENCES

1. Gao, W., Zhu, Y., Wang, Y., Yuan, G. & Liu, J.-M. A review of flexible perovskite oxide ferroelectric films and their application. *J. Materiomics* **6**, 1–16 (2020).
2. Kojima, A., Teshima, K., Shirai, Y. & Miyasaka, T. Organometal halide perovskites as visible-light sensitizers for photovoltaic cells. *J. Am. Chem. Soc.* **131**, 6050–6051 (2009).
3. Snaith, H. J. Perovskites: the emergence of a new era for low-cost, high-efficiency solar cells. *J. Phys. Chem. Lett.* **4**, 3623–3630 (2013).
4. Yin, W.-J. et al. Oxide perovskites, double perovskites and derivatives for electrocatalysis, photocatalysis, and photovoltaics. *Energy Environ. Sci.* **12**, 442–462 (2019).
5. Liu, X.-K. et al. Metal halide perovskites for light-emitting diodes. *Nat. Mater.* **20**, 10–21 (2020).
6. Jiang, P. et al. Pb-free halide perovskites for solar cells, light-emitting diodes, and photocatalysts. *APL Mater.* **10**, 060902 (2022).
7. Brenner, T. M., Egger, D. A., Kronik, L., Hodes, G. & Cahen, D. Hybrid organic-inorganic perovskites: low-cost semiconductors with intriguing charge-transport properties. *Nat. Rev. Mater.* **1**, 1–16 (2016).
8. Fauqué, B. et al. Mesoscopic fluctuating domains in strontium titanate. *Phys. Rev. B* **106**, L140301 (2022).
9. Lee, W. et al. Ultralow thermal conductivity in all-inorganic halide perovskites. *Proc. Natl Acad. Sci. USA* **114**, 8693–8697 (2017).
10. Simoncelli, M., Marzari, N. & Mauri, F. Unified theory of thermal transport in crystals and glasses. *Nat. Phys.* **15**, 809–813 (2019).
11. Poncé, S., Schlipf, M. & Giustino, F. Origin of low carrier mobilities in halide perovskites. *ACS Energy Lett.* **4**, 456–463 (2019).
12. Katan, C., Mohite, A. D. & Even, J. Entropy in halide perovskites. *Nat. Mater.* **17**, 377–379 (2018).
13. Ghosh, D., Welch, E., Neukirch, A. J., Zakhidov, A. & Tretiak, S. Polarons in halide perovskites: a perspective. *J. Phys. Chem. Lett.* **11**, 3271–3286 (2020).
14. Zhao, X.-G., Dalpian, G. M., Wang, Z. & Zunger, A. Polymorphous nature of cubic halide perovskites. *Phys. Rev. B* **101**, 155137 (2020).
15. Zhao, X.-G., Wang, Z., Malyi, O. I. & Zunger, A. Effect of static local distortions vs. dynamic motions on the stability and band gaps of cubic oxide and halide perovskites. *Mater. Today* **49**, 107–122 (2021).
16. Zhao, Y. et al. Lattice thermal conductivity including phonon frequency shifts and scattering rates induced by quartic anharmonicity in cubic oxide and fluoride perovskites. *Phys. Rev. B* **104**, 224304 (2021).
17. Itoh, K., Ochiai, K., Kawaguchi, H., Moriyoshi, C. & Nakamura, E. Structural fluctuations of $SrTiO_3$ in the cubic phase. *Ferroelectrics* **159**, 85–90 (1994).
18. Even, J., Carignano, M. & Katan, C. Molecular disorder and translation/rotation coupling in the plastic crystal phase of hybrid perovskites. *Nanoscale* **8**, 6222–6236 (2016).
19. Marronnier, A. et al. Structural instabilities related to highly anharmonic phonons in halide perovskites. *J. Phys. Chem. Lett.* **8**, 2659–2665 (2017).
20. Yaffe, O. et al. Local polar fluctuations in lead halide perovskite crystals. *Phys. Rev. Lett.* **118**, 136001 (2017).
21. Marronnier, A. et al. Anharmonicity and disorder in the black phases of cesium lead iodide used for stable inorganic perovskite solar cells. *ACS Nano* **12**, 3477–3486 (2018).
22. Liu, J., Phillips, A. E., Keen, D. A. & Dove, M. T. Thermal disorder and bond anharmonicity in cesium lead iodide studied by neutron total scattering and the reverse monte carlo method. *J. Phys. Chem. C* **123**, 14934–14940 (2019).
23. Ferreira, A. C. et al. Direct evidence of weakly dispersed and strongly anharmonic optical phonons in hybrid perovskites. *Commun. Phys.* **3**, 48 (2020).
24. Cohen, A. et al. Diverging expressions of anharmonicity in halide perovskites. *Adv. Mater.* **34**, 2107932 (2022).
25. Lanigan-Atkins, T. et al. Two-dimensional overdamped fluctuations of the soft perovskite lattice in $CsPbBr_3$. *Nat. Mater.* **20**, 977–983 (2021).
26. Hehlen, B. et al. Pseudospin-phonon pretransitional dynamics in lead halide hybrid perovskites. *Phys. Rev. B* **105**, 024306 (2022).
27. Comes, R., Lambert, M. & Guinier, A. The chain structure of $BaTiO_3$ and $KNbO_3$. *Solid State Commun.* **6**, 715–719 (1968).
28. Senn, M. S., Keen, D. A., Lucas, T. C. A., Hriljac, J. A. & Goodwin, A. L. Emergence of long-range order in $BaTiO_3$ from local symmetry-breaking distortions. *Phys. Rev. Lett.* **116**, 207602 (2016).
29. Beecher, A. N. et al. Direct observation of dynamic symmetry breaking above room temperature in methylammonium lead iodide perovskite. *ACS Energy Lett.* **1**, 880–887 (2016).
30. Culbertson, C. M. et al. Neutron total scattering studies of group II titanates ($ATiO_3$, A^{2+} = Mg, Ca, Sr, Ba). *Sci. Rep.* **10**, 3729 (2020).
31. Doherty, T. A. S. et al. Stabilized tilted-octahedra halide perovskites inhibit local formation of performance-limiting phases. *Science* **374**, 1598–1605 (2021).

32. Zacharias, M., Volonakis, G., Giustino, F. & Even, J. Anharmonic lattice dynamics via the special displacement method. *Phys. Rev. B* **108**, 035155 (2023).
33. Hooton, D. LI. a new treatment of anharmonicity in lattice thermodynamics: I. *Lond. Edinb. Dublin Philos. Mag. J. Sci.* **46**, 422–432 (1955).
34. Zacharias, M. & Giustino, F. One-shot calculation of temperature-dependent optical spectra and phonon-induced band-gap renormalization. *Phys. Rev. B* **94**, 075125 (2016).
35. Zacharias, M. & Giustino, F. Theory of the special displacement method for electronic structure calculations at finite temperature. *Phys. Rev. Res.* **2**, 013357 (2020).
36. Saidi, W. A., Poncé, S. & Monserrat, B. Temperature dependence of the energy levels of methylammonium lead iodide perovskite from first-principles. *J. Phys. Chem. Lett.* **7**, 5247–5252 (2016).
37. Allen, P. B. & Heine, V. Theory of the temperature dependence of electronic band structures. *J. Phys. C* **9**, 2305 (1976).
38. Giustino, F. Electron-phonon interactions from first principles. *Rev. Mod. Phys.* **89**, 015003 (2017).
39. Piskunov, S., Heifets, E., Eglitis, R. & Borstel, G. Bulk properties and electronic structure of $SrTiO_3$, $BaTiO_3$, $PbTiO_3$ perovskites: an ab initio HF/DFT study. *Comput. Mater. Sci.* **29**, 165–178 (2004).
40. Ferreira, A. C. et al. Elastic softness of hybrid lead halide perovskites. *Phys. Rev. Lett.* **121**, 085502 (2018).
41. Filip, M. R., Eperon, G. E., Snaith, H. J. & Giustino, F. Steric engineering of metal-halide perovskites with tunable optical band gaps. *Nat. Commun.* **5**, 5757 (2014).
42. Fujii, Y., Hoshino, S., Yamada, Y. & Shirane, G. Neutron-scattering study on phase transitions of $CsPbCl_3$. *Phys. Rev. B* **9**, 4549–4559 (1974).
43. Lahnsteiner, J. & Bokdam, M. Anharmonic lattice dynamics in large thermodynamic ensembles with machine-learning force fields: $CsPbBr_3$, a phonon liquid with Cs rattlers. *Phys. Rev. B* **105**, 024302 (2022).
44. Patrick, C. E., Jacobsen, K. W. & Thygesen, K. S. Anharmonic stabilization and band gap renormalization in the perovskite $CsSnI_3$. *Phys. Rev. B* **92**, 201205 (2015).
45. Kopecký, M., Fábry, J. & Kub, J. X-ray diffuse scattering in $SrTiO_3$ and model of atomic displacements. *J. Appl. Crystallogr.* **45**, 393–397 (2012).
46. Even, J., Pedesseau, L., Jancu, J.-M. & Katan, C. Importance of spin–orbit coupling in hybrid organic/inorganic perovskites for photovoltaic applications. *J. Phys. Chem. Lett.* **4**, 2999–3005 (2013).
47. Yang, Z. et al. Impact of the halide cage on the electronic properties of fully inorganic cesium lead halide perovskites. *ACS Energy Lett.* **2**, 1621–1627 (2017).
48. Kok, D. J. et al. Temperature-dependent optical absorption of $SrTiO_3$. *Phys. Status Solidi (a)* **212**, 1880–1887 (2015).
49. Mannino, G. et al. Temperature-dependent optical band gap in $CsPbBr_3$, $MAPbBr_3$, and $FAPbBr_3$ single crystals. *J. Phys. Chem. Lett.* **11**, 2490–2496 (2020).
50. Sutton, R. J. et al. Cubic or orthorhombic? Revealing the crystal structure of metastable black-phase $CsPbI_3$ by theory and experiment. *ACS Energy Lett.* **3**, 1787–1794 (2018).
51. Stoumpos, C. C. et al. Crystal growth of the perovskite semiconductor $CsPbBr_3$: a new material for high-energy radiation detection. *Cryst. Growth Des.* **13**, 2722–2727 (2013).
52. Schlipf, M. & Giustino, F. Dynamic Rashba-Dresselhaus effect. *Phys. Rev. Lett.* **127**, 237601 (2021).
53. Wiktor, J., Rothlisberger, U. & Pasquarello, A. Predictive determination of band gaps of inorganic halide perovskites. *J. Phys. Chem. Lett.* **8**, 5507–5512 (2017).
54. Fu, M. et al. Unraveling exciton–phonon coupling in individual $FAPbI_3$ nanocrystals emitting near-infrared single photons. *Nat. Commun.* **9**, 3318 (2018).
55. Karakus, M. et al. Phonon–electron scattering limits free charge mobility in methylammonium lead iodide perovskites. *J. Phys. Chem. Lett.* **6**, 4991–4996 (2015).
56. Schlipf, M., Poncé, S. & Giustino, F. Carrier lifetimes and polaronic mass enhancement in the hybrid halide perovskite $CH_3NH_3PbI_3$ from multiphonon fröhlich coupling. *Phys. Rev. Lett.* **121**, 086402 (2018).
57. Lee, H. et al. Electron-phonon physics from first principles using the EPW code. Preprint at https://doi.org/10.48550/arxiv.2302.08085 (2023).
58. Ning, J. et al. Temperature-dependence of the band gap in the all-inorganic perovskite $CsPbI_3$ from room to high temperatures. *Phys. Chem. Chem. Phys.* **24**, 16003–16010 (2022).
59. Zhang, H. et al. Ultrafast relaxation of lattice distortion in two-dimensional perovskites. *Nat. Phys.* **19**, 545–550 (2023).
60. Miyata, K. et al. Large polarons in lead halide perovskites. *Sci. Adv.* **3**, e170121 (2017).
61. Miyata, K. & Zhu, X.-Y. Ferroelectric large polarons. *Nat. Mater.* **17**, 379–381 (2018).
62. Frenzel, M. et al. Nonlinear terahertz control of the lead halide perovskite lattice. *Sci. Adv.* **9**, eadg385 (2023).
63. Giannozzi, P. et al. QUANTUM ESPRESSO: a modular and open-source software project for quantum simulations of materials. *J. Phys. Condens. Matter* **21**, 395502 (2009).
64. Giannozzi, P. et al. Advanced capabilities for materials modelling with Quantum ESPRESSO. *J. Phys. Condens. Matter* **29**, 465901 (2017).
65. Perdew, J. P. et al. Restoring the density-gradient expansion for exchange in solids and surfaces. *Phys. Rev. Lett.* **100**, 136406 (2008).
66. Hamann, D. R. Optimized norm-conserving Vanderbilt pseudopotentials. *Phys. Rev. B* **88**, 085117 (2013).
67. van Setten, M. et al. The PseudoDojo: training and grading a 85 element optimized norm-conserving pseudopotential table. *Comput. Phys. Commun.* **226**, 39–54 (2018).
68. Okazaki, A. & Kawaminami, M. Lattice constant of strontium titanate at low temperatures. *Mater. Res. Bull.* **8**, 545–550 (1973).
69. Kunc, K. & Martin, R. M. in *Ab Initio Calculation of Phonon Spectra* (eds Devreese, J. T., Doren, V. E. & Camp, P. E.) 65–99 (Plenum, 1983).
70. Togo, A. & Tanaka, I. First principles phonon calculations in materials science. *Scr. Mater.* **108**, 1–5 (2015).
71. Gonze, X. & Lee, C. Dynamical matrices, born effective charges, dielectric permittivity tensors, and interatomic force constants from density-functional perturbation theory. *Phys. Rev. B* **55**, 10355–10368 (1997).
72. Perdew, J. P., Ernzerhof, M. & Burke, K. Rationale for mixing exact exchange with density functional approximations. *J. Chem. Phys.* **105**, 9982–9985 (1996).
73. Krukau, A. V., Vydrov, O. A., Izmaylov, A. F. & Scuseria, G. E. Influence of the exchange screening parameter on the performance of screened hybrid functionals. *J. Chem. Phys.* **125**, 224106 (2006).
74. Kresse, G. & Furthmüller, J. Efficiency of ab-initio total energy calculations for metals and semiconductors using a plane-wave basis set. *Comp. Mater. Sci.* **6**, 15–50 (1996).
75. Blöchl, P. E. Projector augmented-wave method. *Phys. Rev. B* **50**, 17953–17979 (1994).
76. Zacharias, M., Scheffler, M. & Carbogno, C. Fully anharmonic nonperturbative theory of vibronically renormalized electronic band structures. *Phys. Rev. B* **102**, 045126 (2020).
77. Ong, S. P. et al. Python materials genomics (pymatgen): a robust, open-source python library for materials analysis. *Comput. Mater. Sci.* **68**, 314–319 (2013).
78. de Ligny, D. & Richet, P. High-temperature heat capacity and thermal expansion of $SrTiO_3$ and $SrZrO_3$ perovskites. *Phys. Rev. B* **53**, 3013–3022 (1996).
79. Allen, P. B., Berlijn, T., Casavant, D. A. & Soler, J. M. Recovering hidden bloch character: unfolding electrons, phonons, and slabs. *Phys. Rev. B* **87**, 085322 (2013).
80. Zheng, F. & Zhang, P. Phonon dispersion unfolding in the presence of heavy breaking of spatial translational symmetry. *Comput. Mater. Sci.* **125**, 218–223 (2016).
81. Zacharias, M. et al. Efficient first-principles methodology for the calculation of the all-phonon inelastic scattering in solids. *Phys. Rev. Lett.* **127**, 207401 (2021).
82. Zacharias, M. et al. Multiphonon diffuse scattering in solids from first principles: application to layered crystals and two-dimensional materials. *Phys. Rev. B* **104**, 205109 (2021).
83. Peng, L.-M., Dudarev, S. & Whelan, M. *High-energy Electron Diffraction and Microscopy* (Oxford University Press, 2004).

ACKNOWLEDGEMENTS

We thank M. Kopecký and J. Fábry for kindly sharing experimental data of $SrTiO_3$ diffuse scattering maps. We also thank D. R. Ceratti for graciously providing data on temperature-dependent band gaps of $CsPbBr_3$ single crystals. M.Z. acknowledges funding from the European Union's Horizon 2020 research and innovation program under the Marie Skłodowska-Curie Grant Agreement No. 899546. This research was also funded by the European Union (project ULTRA-2DPK/HORIZON-MSCA-2022-PF-01 / Grant Agreement No. 101106654). Views and opinions expressed are however those of the authors only and do not necessarily reflect those of the European Union or the European Commission. Neither the European Union nor the granting authority can be held responsible for them. J.E. acknowledges financial support from the Institut Universitaire de France. F.G. was supported by the National Science Foundation under CSSI Grant No. 2103991 and DMREF Grant No. 2119555. The work at institute FOTON and ISCR was supported by the European Union's Horizon 2020 research and innovation program under grant agreement 861985 (PeroCUBE) and grant agreement 899141 (PoLLoC). G.V. acknowledges support from the Agence Nationale pour la Recherche through the CPJ program. We acknowledge that the results of this research have been achieved using the DECI resource Prometheus at CYFRONET in Poland [https://www.cyfronet.pl/] with support from the PRACE aisbl and HPC resources from the Texas Advanced Computing Center (TACC) at The University of Texas at Austin [http://www.tacc.utexas.edu].

AUTHOR CONTRIBUTIONS

M.Z. performed the computational study and wrote the first draft of the manuscript. G.V. performed the hybrid functional calculations. All authors participated in discussions and the final preparation of the manuscript.

COMPETING INTERESTS

The authors declare no competing interests.

ADDITIONAL INFORMATION

Supplementary information The online version contains supplementary material available at https://doi.org/10.1038/s41524-023-01089-2.

Correspondence and requests for materials should be addressed to Marios Zacharias or Jacky Even.

Reprints and permission information is available at http://www.nature.com/reprints

Publisher's note Springer Nature remains neutral with regard to jurisdictional claims in published maps and institutional affiliations.